



OPEN

High-performance parallel tandem MoTe₂/perovskite solar cell based on reduced graphene oxide as hole transport layer

Mohammad Gholipour^{1✉}, Nasrin Solhtalab¹ & Mohammad Hosein Mohammadi²

Recently, the impressive achievements accomplished in multijunction (tandem) perovskite solar cells have triggered a huge research effort to boost their performance. Here, using a three-dimensional (3D) finite element method (FEM) technique, we propose and investigate a parallel tandem PSCs consisting of two absorbing layers of MoTe₂ and CH₃NH₃PbI₃ with cascaded bandgaps to more efficiently use the near-infrared (NIR) solar spectrum. Endowed with a bandgap of about 1 eV, the MoTe₂ layer in conjunction with a CH₃NH₃PbI₃ layer is able to broaden the light absorption range of structure beyond the wavelength of 800 nm, up to 1200 nm. In addition to this, the MoTe₂ material can not only appreciably harvest light even with a thickness as low as 20 nm due to their high absorption coefficient, but also make a perfect band alignment with the CH₃NH₃PbI₃ layer. As a result, the proposed multijunction PCS yields a high power conversion efficiency (PCE) of 18.52% with a V_{OC} of 0.83 V, J_{sc} of 26.25 mA/cm², and FF of 0.84, which is considerably greater than its corresponding single-junction PSCs with PCE, V_{OC}, J_{sc} and FF of, 14.01%, 1.14 V, 15.20 mA/cm², and 0.81, respectively. Furthermore, to mitigate the V_{OC} loss caused by the low bandgap of MoTe₂, we demonstrate an increase in V_{OC} from 0.84 to 0.928 V and in PCE from 18.52% to 20.32%, when we replace a reduced graphene oxide (rGO) layer with Spiro-OMeTAD layer as a hole transport layer (HTL).

Organic–inorganic metal hybrid perovskites have been consistently arousing extraordinary research interest in the photovoltaic community owing to their exceptional semiconductor properties such as facile fabrication process, long diffusion length¹, long carrier lifetime², panchromatic absorption of light³, etc. To date, the maximum power conversion efficiency (PCE) achieved in single-junction perovskite solar cells (PSCs) has been as high as 25.5%¹. So as to further enhance the PCE constrained by the Shockley–Queisser (SQ) limit, some different strategies were pursued, namely, the carrier multiplication effect to harvest the additional energy ($h\nu - E_g$) of photons with energy larger than bandgap (E_g)⁴ and multijunction absorbers to harvest photons with energy smaller than E_g ⁵. Whereas it still is impractical and elusive to gain the PCE via carrier multiplication phenomena, multijunction (tandem) PSCs have successfully achieved the PCE as large as 29.15%⁶. However, inspired by the achievements of counterparts of tandem PSCs, GaAs and GaInP-based multijunction solar cells which have reached a maximum PCE of 38.8%⁷, there is still a burgeoning interest in the further improvement of the multijunction PSC performance. This has spurred the search for new materials and architectures for multijunction PSCs.

Semiconducting transition metal dichalcogenides (TMDs), including MoS₂, MoSe₂, MoTe₂, WS₂, and WSe₂, are emerging as highly impressive absorbers for solar cells owing to their ultrahigh absorption coefficients⁸, mechanical flexibility⁹, high carrier mobility¹⁰, together with an ideal bandgap for photovoltaic applications⁸. Notably, a TMD layer thinner than 20 nm is able to absorb light even ten times larger than well-known direct bandgap semiconductors⁸. While the TMDs, especially MoS₂, have been widely employed as carrier transport layers (HTLs) in the PSCs^{11,12}, there is no report of deriving a benefit from the TMDs absorption capacity in order to improve the light absorption efficiency in PSCs. Although most TMDs have almost the same bandgap magnitude as perovskites, bulk MoTe₂ with a bandgap of around 1 eV would be a complementary absorbing material for perovskite to harvest the near-infrared (NIR) range of sunlight. The strong NIR absorption capability of MoTe₂, along with the absence of dangling bonds at its surface, a property of TMDs which originate from their weak van der Waals (vdW) interlayer interaction, underpin MoTe₂ as a suitable candidate to be heterostructured with perovskite materials for tandem solar cells^{13,14}. Experimentally, the cost-effective chemical and

¹Department of Energy Science, Sungkyunkwan University (SKKU), Suwon, Republic of Korea. ²Department of Electrical and Computer Engineering, Tarbiat Modares University (TMU), Tehran, Iran. ✉email: mgholipoor@g.skku.edu

mechanical exfoliation methods available allow for uniform and homogeneous thin MoTe₂ film preparation^{15,16}. Thus, it would be more valuable to explore the exploitation of MoTe₂ materials as a supportive absorbing layer, to benefit from the MoTe₂ absorption.

Herein, we numerically present and propose a Planar type of parallel multijunction PSCs with an absorbing region made of a thin MoTe₂ and CH₃NH₃PbI₃. The main device is composed of ITO/TiO₂/CH₃NH₃PbI₃/MoTe₂/Spiro-OMeTAD/Ag layers, a configuration that was likewise fabricated with MoS₂¹⁶. The excellently desirable band alignment of MoTe₂ with other layers, along with its high NIR absorption capacity, remarkably paves the way for achieving higher photovoltaic efficiency. By comparing to single-junction PSCs, the proposed device yields an increase in PCE from 14.01 to 18.52%. By performing an accurate numerical analysis of the MoTe₂ thickness-dependent device performance, an optimum thickness of 25 nm was obtained, which is several orders of amplitude thinner than the previous supportive absorbing layers so far reported in multijunction PSCs¹⁷.

Nonetheless, it is a well-established fact that the utilization of a low band gap absorber is detrimental to the open-circuit voltage (V_{OC}) of solar cells owing to the limited electron and hole quasi fermi level separation. Likewise, we have observed a reduction in V_{oc} after turning the structure into a multijunction device. In order to compensate these photovoltage losses, we replace a reduced graphene oxide (rGO) sheet with Spiro-OMeTAD as an HTL to improve the hole extraction and transportation. Outstandingly, the rGO sheet enhances the device V_{OC} and PCE up to 0.928 and 20.32%, respectively. It is noteworthy that the efficacious performance of the rGO layer as both interlayer and charge transport layer has been well proved in PSCs^{18–23}.

Basic equations and models

In this work, we employ a hybrid optical and electrical model to calculate and evaluate the presented structures. We present their traditional formulation (i.e., in the frequency domain) and then discuss the extension to the time domain. A finite element method (FEM) is used to solve the partial differential equations (PDEs).

Optical model. Figure 1A depicts the schematic diagram of our basic planar PSC scheme. From top to bottom, the structure is stacked by a transparent indium tin oxide (ITO) electrode, a compact titanium dioxide (TiO₂) layer, a methylammonium lead iodide perovskite (CH₃NH₃PbI₃) film, an N,N-di(4-methoxyphenyl) amino]-9,9'-spirobifluorene (spiro-OMeTAD) layer, and a silver (Ag) rear electrode. The incident light enters the cell from the ITO layer and is absorbed by the perovskite film to some extent. Also, the incoming light experiences a multireflection because of the rear Ag reflector which gives rise to an absorption enhancement. To quantify the interaction between electromagnetic waves and the layers, as well as the electric field (E) distribution, the Helmholtz equation (represented as follows) was solved:

$$\nabla \times (\nabla \times E) - k_0^2 \epsilon_r E = 0$$

where k_0 is the free space wave number and ϵ_r is the dielectric constant. Clearly, to solve the above equation, one needs all the complex refractive index ($N = n + ik$) of layers as a function of wavelength. Subsequently, the E distribution obtained from solving the above Helmholtz equation enables us to compute the light absorption and carrier generation rate (G_{opt}). The transfer-matrix method (TMM) is applied to estimate G_{opt} in each layer of the structure. The G_{opt} formula is as follows,

$$G_{OPT} = \frac{\epsilon'' E^2}{2\hbar}$$

where \hbar is the reduced Planck constant, and ϵ'' is the imaginary part of the relative permittivity. As the formula obviously indicates, G_{opt} is proportional to the square of the E intensity in a certain wavelength. The total generation rate (G_{tot}) can be calculated by integrating G_{opt} over an incident light wavelength bandwidth.

$$G_{tot} = \int_{\lambda_{min}}^{\lambda_{max}} G_{opt}(\lambda) d(\lambda)$$

The resulting G_{tot} is used for the input of electric model.

Electrical model. The following well-known J–V relation is used to describe electrical characteristics of the present PSCs:

$$J(V) = J_{dark} + J_{sc} = J_0 \left(\exp\left(\frac{eV}{nKT}\right) - 1 \right) - qG_{opt}(L_n + L_p)$$

where J_{dark} depicts the electric current of the PSCs in the absence of light illumination, J_{sc} is photocurrent, e is the electron charge, n is an ideality factor, K is the Boltzmann's constant, and T is the temperature in kelvin. In order to calculate the currents, the following Poisson and continuity equations should be solved across the device:

$$\nabla \cdot (\epsilon_0 \epsilon_r \nabla \phi) = -\rho$$

$$\frac{\partial n}{\partial t} = \frac{1}{q} \nabla_{jn} + G_n - U_N$$

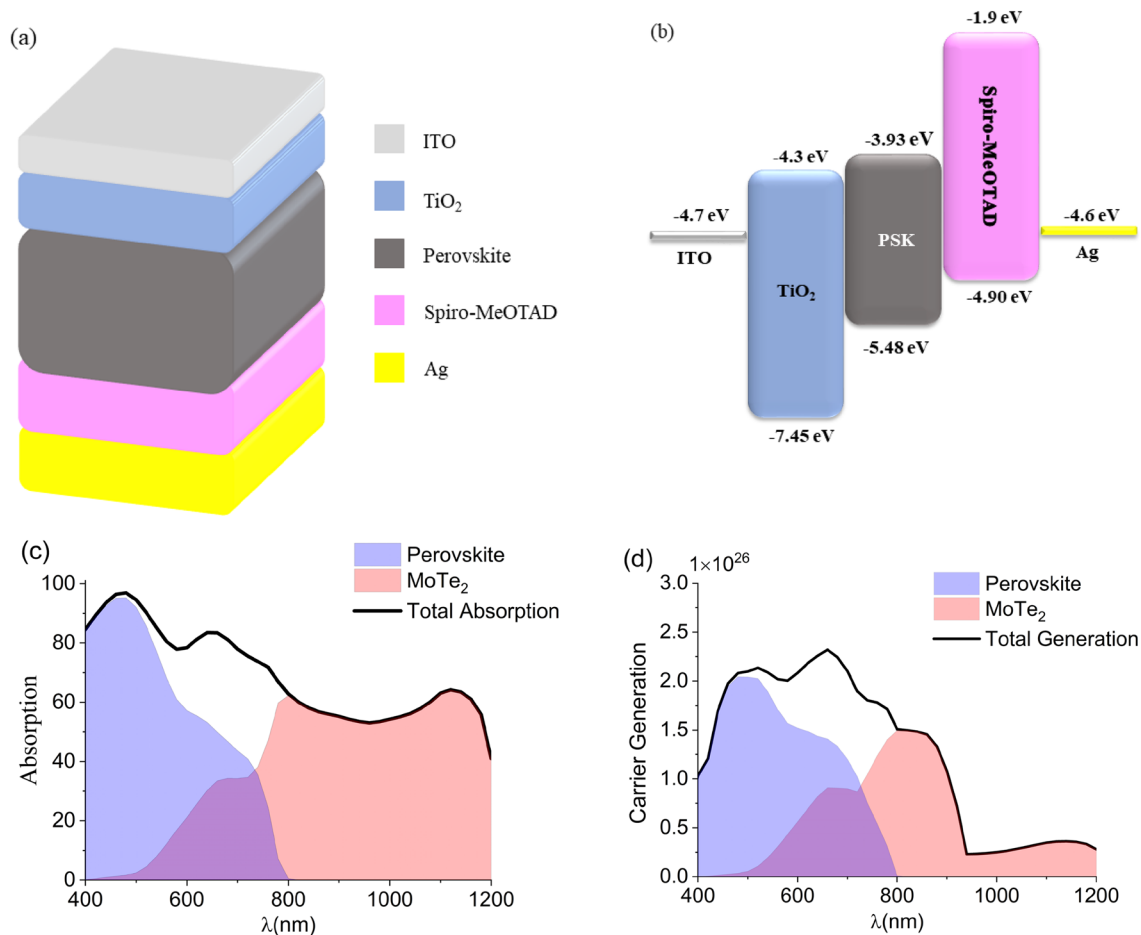


Figure 1. Schematic and energy diagram and device performance. **(a)** The stack structure of the basic PSC designed in this work. **(b)** the band alignment diagram and operation principle of the basic PSC. **(c)** The absorption spectra of the basic PSC, with determining the contribution of each layer. **(d)** the carrier generation rate in absorbing layers as a function of wavelength.

$$\frac{\partial p}{\partial t} = \frac{1}{q} \nabla_{j_p} + G_p - U_p$$

where ϵ_0 is the permittivity of free space, ϕ is the electrostatic potential, ρ is the charge density, and q is the electron charge. Also, the J_n and J_p show the current densities arising from electrons and holes, respectively, the U_n and U_p illustrate the electron and hole recombination rates, respectively, and G_n and G_p are the electron and hole generation rates, respectively. By assuming that every absorbed photon creates one electron–hole pair, G_n and G_p are considered same to the G_{tot} obtained from the optical part.

In this study, the influence of grain boundaries and the carrier recombination at the interfaces between semiconductors are neglected. Additionally, we assume that trap-assisted recombination (SRH) inside bulk materials is the fastest and most dominant recombination mechanism in our devices.

Results and discussion

As mentioned earlier, the reference PSC is made of ITO, TiO_2 , $\text{CH}_3\text{NH}_3\text{PBI}_3$, spiro-OMeTAD, Ag layers, as demonstrated in Fig. 1a. The ITO, TiO_2 , $\text{CH}_3\text{NH}_3\text{PBI}_3$, spiro-OMeTAD, and Ag layers act as the front transparent electrode, electron transport layer (ETL), absorbing layer, hole transport layer (HTL), and back electrode, respectively. Throughout this manuscript, the thickness of ITO, TiO_2 , $\text{CH}_3\text{NH}_3\text{PBI}_3$, spiro-OMeTAD, and Ag layers are fixed at 50, 90, 200, 100, and 100 nm, respectively. Figure 1b exhibits the energy band diagram of components in the structure, approving a favorable band alignment for the electron and hole transfer across the device. Strictly speaking, the sizable valence band offset between perovskite (−5.48 eV) and ETL (−7.45 eV) effectively blocks the hole injection, while their conduction band is nicely aligned for collecting the excited electrons in the perovskite film. Conversely, the band alignment between $\text{CH}_3\text{NH}_3\text{PBI}_3$ (−3.93 eV) and Spiro-OMeTAD (−1.9 eV) makes adequately feasible the hole transfer in the valence band, while it impedes the electron transfer in the conduction band. The input parameters, the values of energy band gap (E_g) and electron affinity (χ) of all components are chosen according to the literature^{17,24,25}, and their values are indexed to the vacuum level. The black curve of Fig. 1c shows the total absorption in the reference PSC. The refractive index data of TiO_2 , $\text{CH}_3\text{NH}_3\text{PBI}_3$, and

Parameters	TiO ₂	PSK	MoTe ₂	Spiro
ϵ_r	9	6.5	13.6	10
N_c (cm ⁻³)	1×10^{19}	1.66×10^{19}	1.6×10^{19}	1.79×10^{19}
N_v (cm ⁻³)	1×10^{19}	5.41×10^{19}	2×10^{19}	2.51×10^{19}
μ_n/μ_p (cm ² /VS)	20/10	50/50	100/25	25/25
χ (eV)	4.1	3.93	3.9	1.9
E_g (eV)	3.2	1.55	1.03	3.0
NA (cm ⁻³)	–	–	5×10^{15}	5×10^{19}
ND (cm ⁻³)	5×10^{18}	1×10^{12}	–	–
τ_n/τ_p	5/2	8/8	5/5	15/15

Table 1. The input simulation parameters.

spiro-OMeTAD are taken from the references^{26–28}. The blue shaded area of Fig. 1c manifests the absorption spectra of PSK in the structure. It is clear that the perovskite layer can only absorb sunlight over 300–800 nm due to its bandgap (1.55 eV), so all NIR light is wasted. To push light absorption beyond the visible range, an ultrathin MoTe₂ layer is placed below the perovskite film. The bulk MoTe₂ semiconductor endowed with a small indirect bandgap of about 1.0 eV²⁹ is able to extend light absorption to wavelengths up to 1200 nm, as is indicated by the pink shaded region of Fig. 1c. Besides an indirect bandgap, the bulk MoTe₂ enjoys two dominant direct excitonic gaps, termed A and B, around 1.2 and 1.5 eV, respectively^{30,31}, which specify its absorption peaks, as appeared in Fig. 1c. Subsequently, the black curve in Fig. 1d shows the total G_{opt} in the device. It confirms an efficient light absorption led to carrier generation over the NIR range. The blue and pink-shaded areas of Fig. 1d unveil the contribution of PSK and MoTe₂ layers, respectively, to the total G_{opt} . Quantitatively, the PSK and MoTe₂ layers contribute about 61% and 39% of carrier generation, respectively. This carrier generation enhancement by the MoTe₂ layer could be promising for cell performance improvement. Furthermore, the MoTe₂ layer like other TMD materials can play further advantageous roles in boosting the device performance. The utility of TMDs in PSCs has been broadened to facilitate efficient carrier transport³², prolong the stability¹⁶, and so on³³. Hence, these advantages accompanied by their low cost and easy preparation process—mechanically exfoliation and transfer into a device, affirm their effectiveness in a PSK efficiency enhancement.

In this simulation, the refractive index of bulk MoTe₂ was obtained from the Ref³⁴. Also, in all calculations, the input light source is conformed to the AM1.5G spectrum. The wavelength bandwidth is chosen from 300 to 1200 nm in a resolution of as much as 20 nm. The periodic boundary condition (PBC) is used for each side of the insulating region in the structures and the Au layer sides are set to a perfect electric conductor (PEC). The bottom and top contacts are considered ideal ohmic and Schottky with a surface recombination velocity of 107 cm/s, respectively. Furthermore, a swept mesh is applied to more precisely resolve the fields around the thin layer. Table 1 includes all optical and electrical input values used in the simulations. Herein, ϵ_r is dielectric constant, N_c and N_v are effective density of states of conduction and valence bands, μ_n and μ_p are electron and hole mobilities, χ is electron affinity, E_g is bandgap energy, N_A and N_D are acceptor and donor densities, and τ_n and τ_p are electron and hole lifetimes, respectively. The MoTe₂ materials are known to be naturally P-doped³⁵. In addition, in the bulk limit, the semiconducting TMDs bear photogenerated carrier lifetimes up to a few nanoseconds^{36,37}.

The current density–voltage (J–V) characteristics of our reference PSC under one sun condition are demonstrated in Fig. 2a. The PSC shows a PCE of 14.01%, with J_{sc} of 15.20 mA/cm², V_{oc} of 1.14 V, and FF of 0.81. Benefiting the NIR light absorbed in the MoTe₂ layer, J_{sc} considerably increases by 26.2 mA/cm² in the multijunction PSC with an optimized thickness of MoTe₂. But, the V_{oc} drops to 0.84 V due to the electron and hole quasi fermi level separation is now restricted by the MoTe₂ bandgap. Altogether, notwithstanding the V_{oc} is destroyed after inserting the MoTe₂ layer, the enhancement of J_{sc} is highly predominated over the V_{oc} reduction, leading to a noticeable increase in PCE from 14.01% to 18.52%. This PCE increase is also contributed by a suitable band alignment between MoTe₂ and the perovskite layer and HTL, as indicated in Fig. 2b. Indeed, the desired band alignment between absorbing layers can effectively mitigate V_{oc} loss in multijunction PSCs as a result of charge transport improvement and charge recombination reduction³⁸. In order to provide a broader perspective on the TMDs capability for light absorption, we compare the absorption spectrum of the present structure with when the MoTe₂ layer was replaced by three other TMDs, WSe₂, MoSe₂, and MoS₂, as illustrated in Fig. 2c. The refractive index and band structure parameters of WSe₂, MoSe₂, and MoS₂ are obtained from the literature^{34,39–41}. While all TMDs show strong light–matter interaction under light illumination, their bandgaps cover a broad range from 1–2 eV⁴². Herein, WSe₂ and MoSe₂ with the bandgap around 1.3 eV can absorb a wider spectrum of light compared to MoS₂ with a bandgap of 1.45 eV. Of these, MoTe₂ clearly is more able to absorb NIR light, making it the best choice to be cascaded with the PSK. Figure 2d,e exhibit the interaction between the light electric fields and different layers at the wavelength of 600 and 1000 nm. One can see that the MoTe₂ layer interacts with light when the wavelength is set to 1000 nm, whereas its contribution to light absorption in the visible wavelength of 600 nm is negligible. It is also worth knowing that the utilization of TMDs in PSCs has shown successful outcomes to enhance stability^{16,43}. On the other side, TMDs in each thickness can be easily prepared through environment-insensitive and non-destructive approaches such as dry or liquid-phase exfoliation¹⁶, then transferred by dry or wet methods. Thus, a combination of PSK materials and TMDs can potentially improve PSC performance, not only photovoltaic operation but also stability.

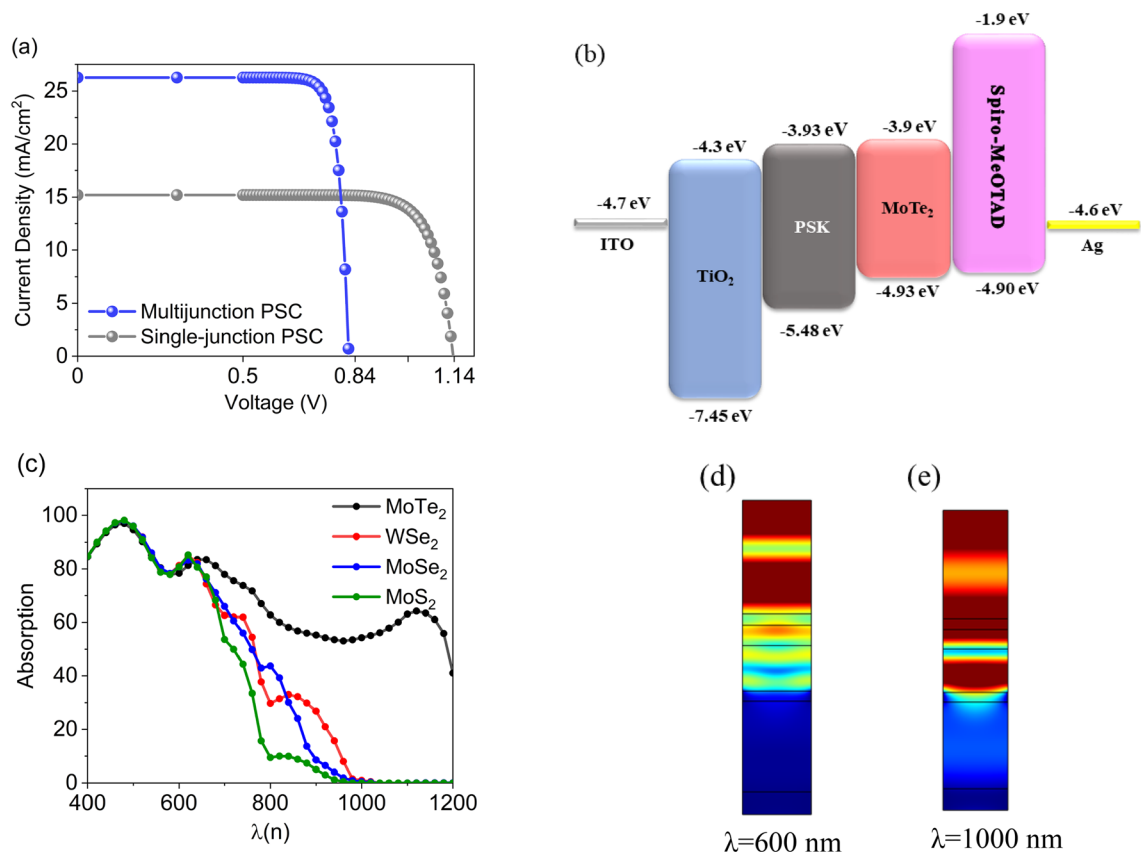


Figure 2. The single and multijunction PSC performance. **(a)** Current density–voltage (J–V) curve of the single PSC and multijunction PSC including MoTe₂. **(b)** The band alignment diagram of multijunction PSC. **(c)** The absorption spectra of the structure for different TMDs including MoTe₂, WSe₂, MoSe₂, and MoS₂. **(d)** and **(e)** The normalized electric field distribution at the wavelengths of 600 and 1000 nm, respectively.

To achieve the multijunction PSC peak performance, an analysis of the cell performance dependence on the MoTe₂ thickness has been carried out, while other input parameters in Table 1 are left unchanged. According to Fig. 3, the absorption, carrier generation, and photovoltaic parameters of the cell change as the MoTe₂ thickness increase from 5 to 100 nm. Figure 3a exhibits the absorption spectra of four different thicknesses of the MoTe₂ layer inside the multijunction PSC. As expected, the thicker the MoTe₂ layer, the more light absorption in the MoTe₂ layer. However, the light absorption rate becomes slower as the MoTe₂ thickness increases, until it reaches saturation at a certain thickness. Even though too much light is absorbed by the MoTe₂ at the longer wavelengths around 1100 nm, the carrier generation is poor at such wavelengths, as illustrate in Fig. 3b. This can be ascribed to resonant cavity effect and interference that play a role in absorption spectra, but do not exert any influence on carrier generation. As shown in Fig. 3c,d, photovoltaic parameters of the cell, PCE, J_{sc}, V_{oc}, and FF vary with the MoTe₂ thickness. With increasing MoTe₂ layer thickness, the J_{sc} gradually increases until it reaches a point of saturation. Conversely, the V_{oc} reduces as the MoTe₂ thickness increases. The V_{oc} initially experiences a quick decrease and then the decrease rate becomes slower with the increase of MoTe₂ thickness. The decreasing V_{oc} value can be assigned to an increase in charge carrier recombination in the thicker absorbing layer and to the increased series resistance⁴⁴. When the absorbing layer thickness is smaller than the carrier diffusion length, the carrier recombination rate significantly diminishes, resulting in a sharp increase in V_{oc}. On the other hand, after a distance as much as carrier diffusion length, a V_{oc} reduction occurs arising from the carrier recombination increase. Also, it is worth noting that the FF parameter has a negligible dependency on the MoTe₂ thickness. Consequently, as indicated in the Fig. 3d, the PCE initially undergoes a relatively intense increase in the response to both V_{oc} and J_{sc} sharp changes in the thinner MoTe₂ thicknesses and then reaches a maximum (~18.52%) at the MoTe₂ thickness of 25 nm, and subsequently, it drops off as the J_{sc} increase is saturated.

In order to compensate the destructive effect of parallelly stacking low and high bandgap materials, we replace the spiro layer with a 60 nm rGO layer to improve the carrier transfer. Arguably, graphene oxide (GO) and rGO can provide multi-benefit to PSCs, namely, the improvement of stability, electrical, and thermal conductivity⁴⁵. Hence, the materials were widely used for different functions in PSCs such as carrier transport layers, interlayers, and transparent conductive oxides. Here, the GO layer is selected to insert as a HTL due to its well-aligned bandstructure with the adjacent layers band edges. The electronic energy band parameters of rGO are obtained from the Ref⁴⁶. As illustrated in the Fig. 4a, the utility of rGO as HTL notably improves both FF and Voc up to

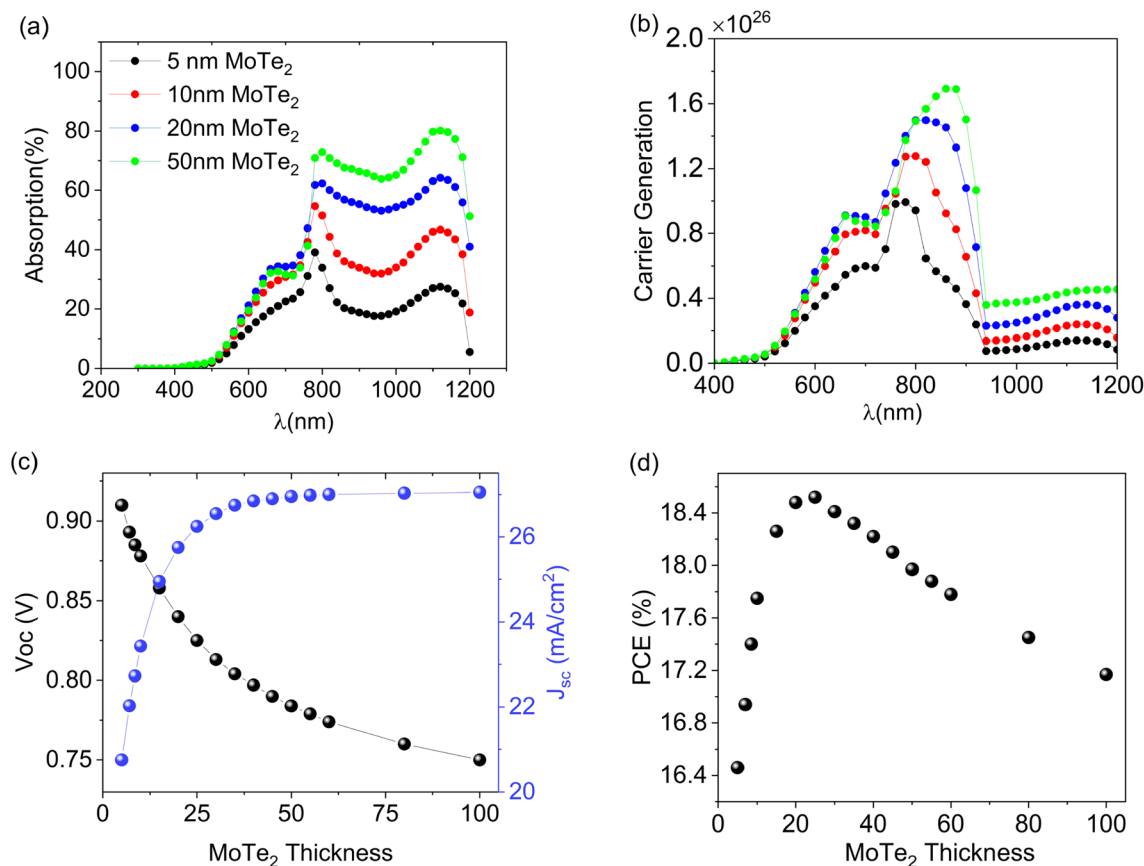


Figure 3. The multijunction PSC performance dependence on MoTe₂ thickness. **(a)** The absorption spectra of the MoTe₂ film with different thicknesses. **(b)** The carrier generation inside the different thicknesses of the MoTe₂ layer. **(c)** The black and blue curves represent the dependence of V_{OC} and J_{SC} on MoTe₂ thickness, respectively. **(d)** The dependence of PCE on MoTe₂ thickness.

0.89 and 0.928, respectively, in the comparison with the multijunction PSC without the rGO layer. Consequently, it yields a PCE as high as 20.32, around 1.77% larger than the multijunction PSC with spiro HTL. The significant improvement of photovoltaic performance in rGO-based multijunction PSC is devoted to more efficient charge transport and better energy band alignment, alongside a reduction in the increased series resistance owing to the expected charge recombination reduction at the interface.

Figure 4b compares the photovoltaic performance of multijunction PSC with different HTLs including Spiro, PTAA, rGO, and CuS materials. The input parameters of these materials are tabulated in Table 2. The rGO layer acts as HTL better than other materials due to its high hole mobility⁴⁷, along with a nice band alignment with MoTe₂. Conversely, CuS is not well energetically aligned with MoTe₂, leading a V_{OC} reduction. The band diagram of multijunction PSC with different HTLs is shown in the Fig. 4c.

Conclusion

In summary, the significant successes achieved in multijunction (tandem) PSCs have intensified scientific efforts to address existing challenges and enhance their current performance. In this direction, we designed and proposed an n-i-p multijunction perovskite solar cell made of ITO/TiO₂/CH₃NH₃PbI₃/MoTe₂/Spiro-OMeTAD/Ag layers, including two absorbers, the CH₃NH₃PbI₃ and MoTe₂, with cascaded bandgaps to absorb a wider solar spectrum. The MoTe₂ layer with a bandgap around 1 eV enables us to harvest photons with energies smaller than the perovskite bandgap. The calculated results show an appreciable increase in the perovskite solar cell efficiency originating from the short circuit current, compared to the cell without MoTe₂. Nevertheless, in a sharp contrast to the short circuit current, stacking the absorbers with different bandgaps has led to a fall in the open circuit voltage because of hole transport deterioration in the absorbing area. In order to alleviate the unavoidable issue, we inserted a graphene oxide layer with a thickness of 1.5 nm. Consequently, we observed that the open circuit voltage increases as much as 0.1 eV, leading to an efficiency improvement from 18.52% to 20.32%. Both MoTe₂ and graphene oxide layers energy bandstructure are perfectly matched with their nearby layers band edges, allowing for achieving a high performance. It is also important to mention that the MoTe₂ and graphene oxide layers chosen in this research have been experimentally utilized for various functions, such as stability improvement, transport layers, etc.

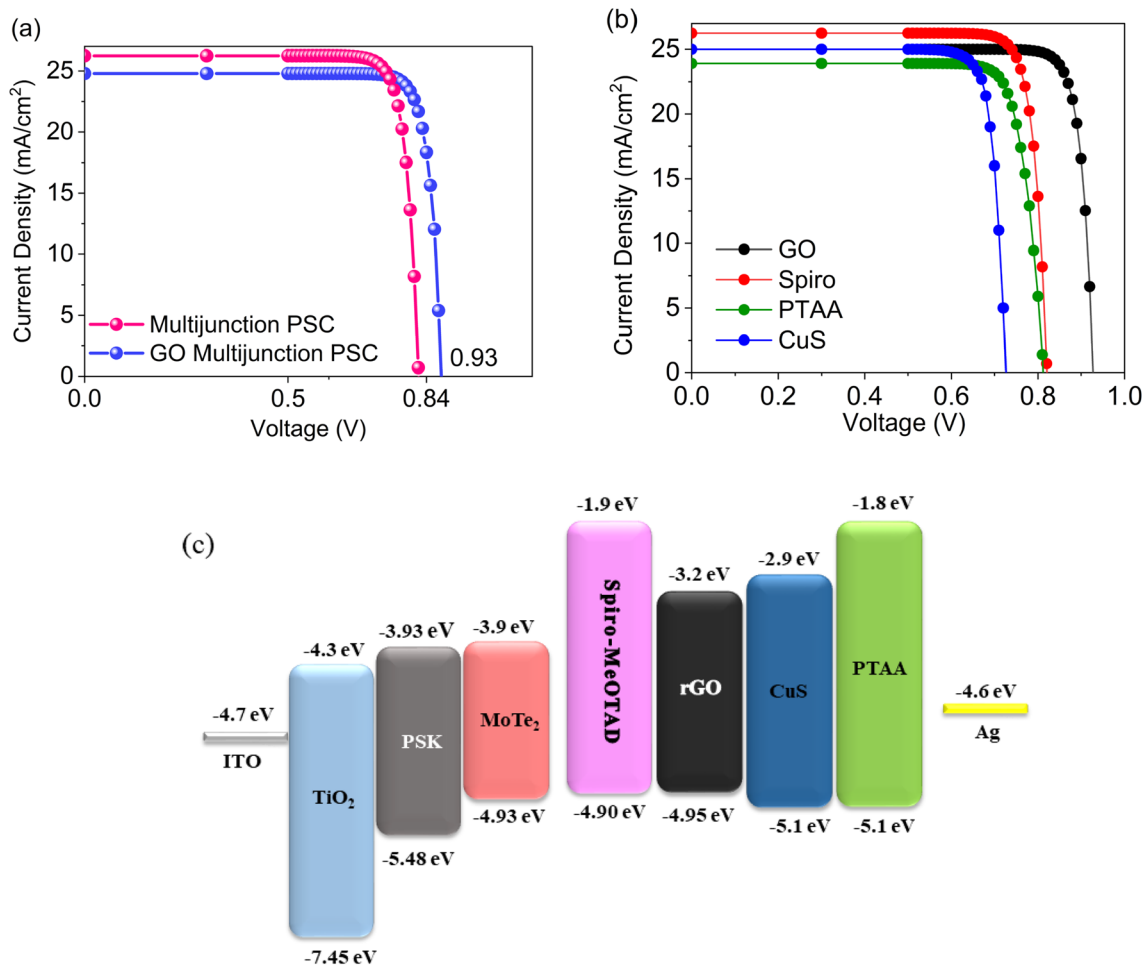


Figure 4. The multijunction PSC performance with and without rGO. **(a)** Current density–voltage (J–V) curve of the multijunction PSC performance with sprio and without rGO HTLs. **(b)** Current density–voltage (J–V) curve of the multijunction PSC with different HTL including Spiro, PTAA, rGO, and CuS. **(c)** Band alignment between the layers of multijunction PSC and the proposed HTLs.

Parameters	rGO	PTAA	CuS	Spiro
ϵ_r	25	3	2.5	3
N_c (cm ⁻³)	2.5×10^{18}	2.5×10^{18}	2.5×10^{18}	2.5×10^{18}
N_v (cm ⁻³)	1.8×10^{19}	1.8×10^{19}	1.8×10^{19}	1.8×10^{19}
μ_n/μ_p (cm ² /VS)	372/372	$5 \times 10^{-3}/5 \times 10^{-3}$	$1 \times 10^{-3}/1 \times 10^{-3}$	$10^{-3}/10^{-3}$
χ (eV)	3.2	1.8	2.9	1.9
E_g (eV)	1.75	3.3	2.2	3.0
NA (cm ⁻³)	5×10^{19}	5×10^{19}	5×10^{19}	5×10^{19}
ND (cm ⁻³)	–	–	–	–
τ_n/τ_p (ns)	3/3	0.48/0.48	5/5	7.1/7.1

Table 2. The input simulation parameters.

Data availability

The datasets used and/or analyzed during the current study are available from the corresponding author on reasonable request.

Received: 15 September 2022; Accepted: 23 November 2022

Published online: 28 November 2022

References

- Dong, Q. *et al.* Electron-hole diffusion lengths > 175 μm in solution-grown $\text{CH}_3\text{NH}_3\text{PbI}_3$ single crystals. *Science* **347**, 967–970 (2015).
- Chen, Y. *et al.* Extended carrier lifetimes and diffusion in hybrid perovskites revealed by Hall effect and photoconductivity measurements. *Nat. Commun.* **7**, 1–9 (2016).
- Liu, M., Johnston, M. B. & Snaith, H. J. Efficient planar heterojunction perovskite solar cells by vapour deposition. *Nature* **501**, 395–398 (2013).
- de Weerd, C. *et al.* Efficient carrier multiplication in CsPbI_3 perovskite nanocrystals. *Nat. Commun.* **9**, 1–9 (2018).
- Wang, R. *et al.* Prospects for metal halide perovskite-based tandem solar cells. *Nat. Photonics* **15**, 411–425 (2021).
- Al-Ashouri, A. *et al.* Monolithic perovskite/silicon tandem solar cell with > 29% efficiency by enhanced hole extraction. *Science* **370**, 1300–1309 (2020).
- Hörantner, M. T. *et al.* The potential of multijunction perovskite solar cells. *ACS Energy Lett.* **2**, 2506–2513 (2017).
- Nassiri Nazif, K. *et al.* High-specific-power flexible transition metal dichalcogenide solar cells. *Nat. Commun.* **12**, 1–9 (2021).
- Velusamy, D. B. *et al.* Flexible transition metal dichalcogenide nanosheets for band-selective photodetection. *Nat. Commun.* **6**, 1–11 (2015).
- Li, H., Huang, J. K., Shi, Y. & Li, L. J. Toward the growth of high mobility 2D transition metal dichalcogenide semiconductors. *Adv. Mater. Interfaces* **6**, 1900220 (2019).
- You, P., Tang, G. & Yan, F. Two-dimensional materials in perovskite solar cells. *Mater. Today Energy* **11**, 128–158 (2019).
- Kohnehpoushi, S., Nazari, P., Nejand, B. A. & Eskandari, M. MoS_2 : a two-dimensional hole-transporting material for high-efficiency, low-cost perovskite solar cells. *Nanotechnology* **29**, 205201 (2018).
- Farmanbar, M. & Brocks, G. First-principles study of van der Waals interactions and lattice mismatch at MoS_2 /metal interfaces. *Phys. Rev. B* **93**, 085304 (2016).
- Siao, M. *et al.* Two-dimensional electronic transport and surface electron accumulation in MoS_2 . *Nat. Commun.* **9**, 1–12 (2018).
- Dasgupta, U., Chatterjee, S. & Pal, A. J. Thin-film formation of 2D MoS_2 and its application as a hole-transport layer in planar perovskite solar cells. *Sol. Energy Mater. Sol. Cells* **172**, 353–360 (2017).
- Liang, M. *et al.* Improving stability of organometallic-halide perovskite solar cells using exfoliation two-dimensional molybdenum chalcogenides. *npj 2D Mater. Appl.* **4**, 1–8 (2020).
- Solhtalab, N., Mohammadi, M. H., Eskandari, M. & Fathi, D. Efficiency improvement of half-tandem CIGS/perovskite solar cell by designing nano-prism nanostructure as the controllable light trapping. *Energy Rep.* **8**, 1298–1308 (2022).
- Park, M.-A. *et al.* Bifunctional graphene oxide hole-transporting and barrier layers for transparent bifacial flexible perovskite solar cells. *ACS Appl. Energy Mater.* **4**, 8824–8831 (2021).
- Zibouche, N., Volonakis, G. & Giustino, F. Graphene oxide/perovskite interfaces for photovoltaics. *J. Phys. Chem. C* **122**, 16715–16726 (2018).
- Wu, Z. *et al.* Efficient planar heterojunction perovskite solar cells employing graphene oxide as hole conductor. *Nanoscale* **6**, 10505–10510 (2014).
- Han, G. S. *et al.* Reduced graphene oxide/mesoporous TiO_2 nanocomposite based perovskite solar cells. *ACS Appl. Mater. Interfaces* **7**, 23521–23526 (2015).
- Yeo, J.-S. *et al.* Highly efficient and stable planar perovskite solar cells with reduced graphene oxide nanosheets as electrode interlayer. *Nano Energy* **12**, 96–104 (2015).
- Palma, A. L. *et al.* Reduced graphene oxide as efficient and stable hole transporting material in mesoscopic perovskite solar cells. *Nano Energy* **22**, 349–360 (2016).
- Albargi, H., Umar, A. & Shkir, M. Enhanced photoresponsivity of anatase titanium dioxide (TiO_2)/nitrogen-doped graphene quantum dots (N-GQDs) heterojunction-based photodetector. *Adv. Compos. Hybrid Mater.* **4**, 1354–1366 (2021).
- Hu, Z. *et al.* Effects of heteroatom substitution in spiro-bifluorene hole transport materials. *Chem. Sci.* **7**, 5007–5012 (2016).
- Sarkar, S. *et al.* Hybridized guided-mode resonances via colloidal plasmonic self-assembled grating. *ACS Appl. Mater. Interfaces* **11**, 13752–13760 (2019).
- Du, Q. G., Shen, G. & John, S. Light-trapping in perovskite solar cells. *AIP Adv.* **6**, 065002 (2016).
- Filipić, M. *et al.* $\text{CH}_3\text{NH}_3\text{PbI}_3$ perovskite/silicon tandem solar cells: characterization based optical simulations. *Opt. Express* **23**, A263–A278 (2015).
- Ruppert, C., Aslan, O. B. & Heinz, T. F. Optical properties and band gap of single- and few-layer MoTe_2 crystals. *Nano Lett.* **14**, 6231–6236 (2014).
- Arora, A. *et al.* Zeeman spectroscopy of excitons and hybridization of electronic states in few-layer WSe_2 , MoSe_2 and MoTe_2 . *2D Materials* **6**, 015010 (2018).
- Arora, A. *et al.* Interlayer excitons in a bulk van der Waals semiconductor. *Nat. Commun.* **8**, 1–6 (2017).
- Ray, R., Sarkar, A. S. & Pal, S. K. Improving performance and moisture stability of perovskite solar cells through interface engineering with polymer-2D MoS_2 nanohybrid. *Sol. Energy* **193**, 95–101 (2019).
- Cao, J. *et al.* Enhanced performance of planar perovskite solar cells induced by van der Waals epitaxial growth of mixed perovskite films on WS_2 flakes. *Adv. Func. Mater.* **30**, 2002358 (2020).
- Beal, A. & Hughes, H. Kramers-Kronig analysis of the reflectivity spectra of 2H- MoS_2 , 2H- MoSe_2 and 2H- MoTe_2 . *J. Phys. C: Solid State Phys.* **12**, 881 (1979).
- Pan, S., Ceballos, F., Bellus, M. Z., Zereszki, P. & Zhao, H. Ultrafast charge transfer between MoTe_2 and MoS_2 monolayers. *2D Materials* **4**, 015033 (2016).
- Shi, H. *et al.* Exciton dynamics in suspended monolayer and few-layer MoS_2 2D crystals. *ACS Nano* **7**, 1072–1080 (2013).
- Wang, H., Zhang, C. & Rana, F. Surface recombination limited lifetimes of photoexcited carriers in few-layer transition metal dichalcogenide MoS_2 . *Nano Lett.* **15**, 8204–8210 (2015).
- Wu, M.-C. *et al.* Enhancing the efficiency of perovskite solar cells using mesoscopic zinc-doped TiO_2 as the electron extraction layer through band alignment. *J. Mater. Chem. A* **6**, 16920–16931 (2018).
- Zhang, C. *et al.* Systematic study of electronic structure and band alignment of monolayer transition metal dichalcogenides in Van der Waals heterostructures. *2D Materials* **4**, 015026 (2016).
- Gu, H. *et al.* Layer-dependent dielectric and optical properties of centimeter-scale 2D WSe_2 : evolution from a single layer to few layers. *Nanoscale* **11**, 22762–22771 (2019).
- Ermolaev, G. A. *et al.* Broadband optical properties of monolayer and bulk MoS_2 . *npj 2D Mater. Appl.* **4**, 1–6 (2020).
- Ansari, N. & Ghorbani, F. Light absorption optimization in two-dimensional transition metal dichalcogenide van der Waals heterostructures. *JOSA B* **35**, 1179–1185 (2018).
- Karimipour, M., Khazraei, S., Kim, B. J., Boschloo, G. & Johansson, E. M. Efficiency and stability enhancement of perovskite solar cells utilizing a thiol ligand and MoS_2 (100) nanosheet surface modification. *ACS Appl. Energy Mater.* **4**, 14080–14092 (2021).
- Lu, H., Gan, X., Mao, D., Jia, B. & Zhao, J. Flexibly tunable high-quality-factor induced transparency in plasmonic systems. *Sci. Rep.* **8**, 1–9 (2018).
- Milić, J. V., Arora, N., Dar, M. I., Zakeeruddin, S. M. & Grätzel, M. Reduced graphene oxide as a stabilizing agent in perovskite solar cells. *Adv. Mater. Interfaces* **5**, 1800416 (2018).

46. Agresti, A. *et al.* Graphene–perovskite solar cells exceed 18% efficiency: A stability study. *Chemsuschem* **9**, 2609–2619 (2016).
47. Bhaumik, A. *et al.* Reduced graphene oxide thin films with very large charge carrier mobility using pulsed laser deposition. *J. Mater. Sci. Eng* **6**, 1–11 (2017).

Author contributions

M.G: main contribution to the conception, wrote the simulation algorithm, design of the work, analysis and interpretation of data, wrote the main manuscript and prepared figures. N.S: significant contribution to the conception, interpretation of data, substantively revised it, wrote some parts of the manuscript. M.H.M: Conceptualization, provided the simulation algorithm, review.

Competing interests

The authors declare no competing interests.

Additional information

Correspondence and requests for materials should be addressed to M.G.

Reprints and permissions information is available at www.nature.com/reprints.

Publisher's note Springer Nature remains neutral with regard to jurisdictional claims in published maps and institutional affiliations.



Open Access This article is licensed under a Creative Commons Attribution 4.0 International License, which permits use, sharing, adaptation, distribution and reproduction in any medium or format, as long as you give appropriate credit to the original author(s) and the source, provide a link to the Creative Commons licence, and indicate if changes were made. The images or other third party material in this article are included in the article's Creative Commons licence, unless indicated otherwise in a credit line to the material. If material is not included in the article's Creative Commons licence and your intended use is not permitted by statutory regulation or exceeds the permitted use, you will need to obtain permission directly from the copyright holder. To view a copy of this licence, visit <http://creativecommons.org/licenses/by/4.0/>.

© The Author(s) 2022